nature research

https://doi.org/10.1038/s41561-020-00653-5

## Supplementary information

# Distinct slab interfaces imaged within the mantle transition zone

In the format provided by the authors and unedited

Supplementary Information for

# Distinct slab interfaces imaged within the mantle transition zone

Xin Wang[1,2], Qi-Fu Chen[1,3,*], Fenglin Niu[4,5,*], Shengji Wei[6,7], Jieyuan Ning[8], Juan Li[1,3], Weijun Wang[9], Johannes Buchen[2], Lijun Liu[10]

[1] Key Laboratory of Earth and Planetary Physics, Institute of Geology and Geophysics, Chinese Academy of Sciences

[2] Seismological Laboratory, California Institute of Technology

[3] College of Earth and Planetary Sciences, University of Chinese Academy of Sciences

[4] Department of Earth Science, Rice University

[5] State Key Laboratory of Petroleum Resources and Prospecting, and Unconventional Petroleum Research Institute, China University of Petroleum at Beijing

[6] Earth Observatory of Singapore, Nanyang Technological University

[7] Asian School of Environment, Nanyang Technological University

[8] School of Earth and Space Sciences, Peking University

[9] Institute of Earthquake Forecasting, China Earthquake Administration

[10] Department of Geology, University of Illinois Urbana-Champaign

Correspondence to: chenqf@mail.iggcas.ac.cn (Q-F. C.);niu@rice.edu (F. N.)

## Introduction

This supporting material provides additional information on results, uncertainty analysis, and 2D waveform simulations. Structures of the supplementary material are shown as below.

**Section S1:** Distribution of Ps piercing points at MTZ depth

**Section S2:** Comparison of our CCP stacking images and the tomography studies

**Section S3:** Noise level on the CCP stacking image

**Section S4:** Side-lobes on RFs caused by data processing

**Section S5:** Shallow structures' effect on MTZ RF study

**Section S6:** 2D synthetic tests using tomography and geothermal models

**Figs. S1 to S12**

## 1. Distribution of Ps piercing points at MTZ depth

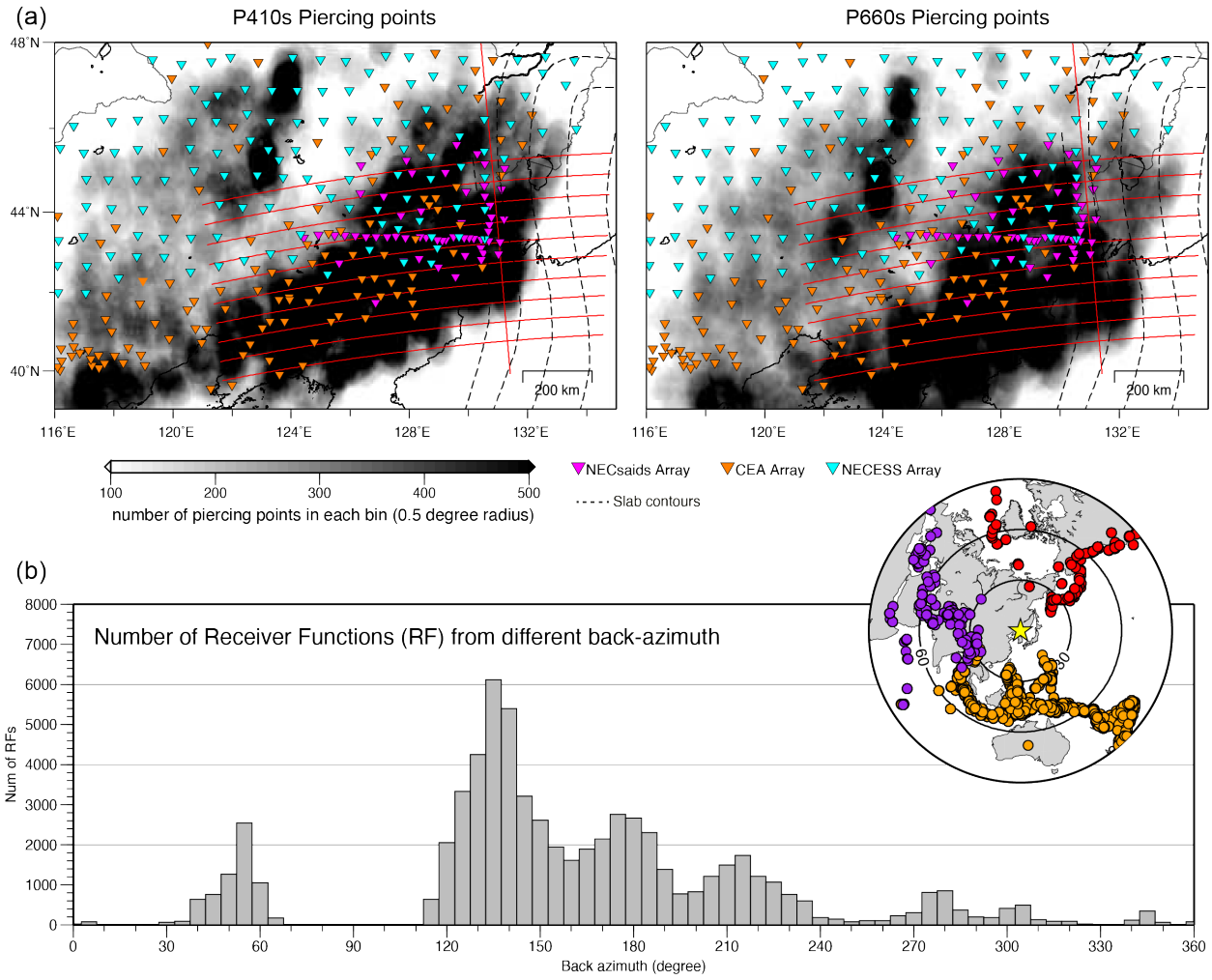


**Figure S1. (a)** Maps showing the density distribution of P410s and P660s piercing located within a bin with a 0.5 radius. The thin red lines show the location of profiles shown in Main Text and Extended Data. **(b)** The histogram shows the number of receiver functions from different back azimuth. As the majority of earthquakes are coming from the south, the piercing points of P410s and P660s are mostly distributed in the region south of 45°N.

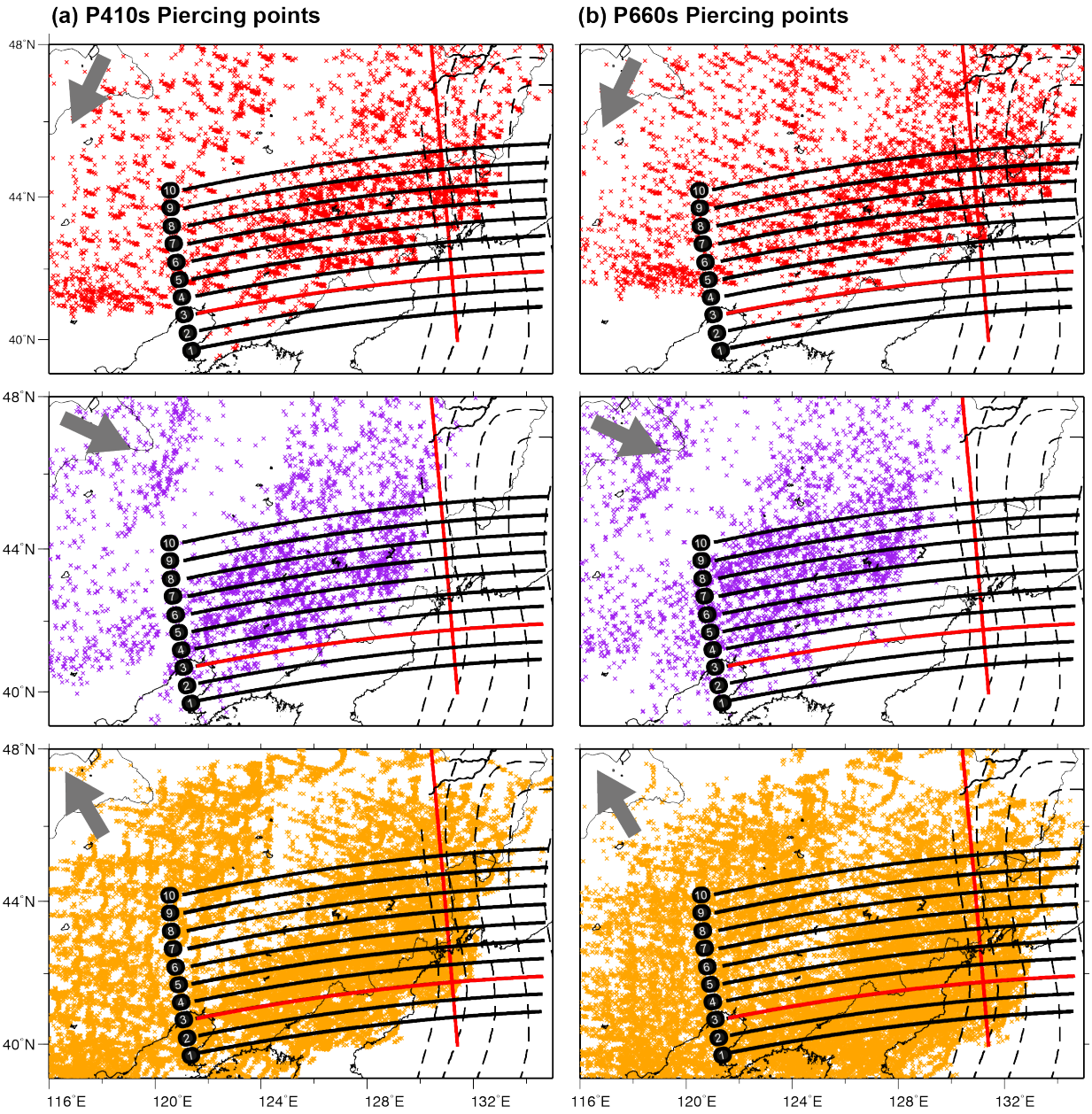


**Fig. S2.** Piercing points of P410s and P660s, colored by their back azimuth. See Fig. S1b for the legend. It should be noted that the phases X1 and X2 are mostly sampled by the earthquakes coming from a narrow back azimuth (120-180 degrees), thus, the dipping structure effect has been significantly reduced. Note that even though the dense linear array of NECESSArray is located at a latitude of ~43.5°, the piercing points of P410s and P660s are shifted laterally from the station by ~ 150 km and ~ 250 km, respectively.

## 2. Comparison of our CCP stacking images and the tomography studies

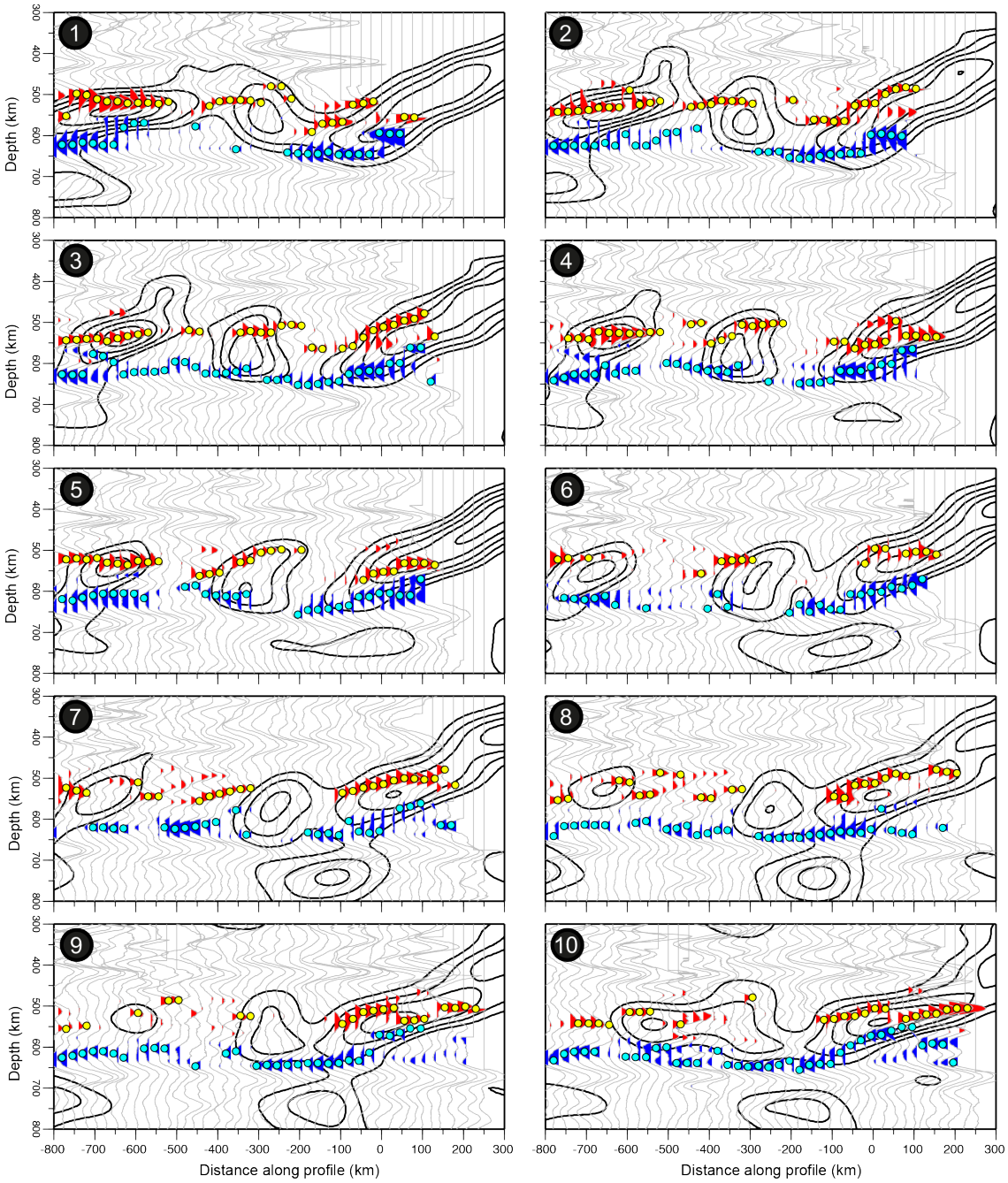


**Fig. S3.** Superimposition of the slab contours on the CCP stacking images (Extended Data Fig. 2 and Fig. 3), where the signals related to the phases X1 and X2 are highlighted in red and blue, respectively. The locations and the depths of the phases X1 (yellow dots) and X2 (cyan dots) are then extracted to construct the cross-correlation analyze in Fig. 4 in Extended Data. Note that there are complexities and uncertainties in both reflectivity structure and tomography studies.

## 3. Noise level on the CCP stacking image

We use a bootstrapping resampling approach[1] to estimate the noise level on the CCP stacking images. We choose the profile A shown in the main text as an example. During the CCP stacking procedure, for each bin, we randomly select n traces of RFs from the original database, allowing duplicates (n =0.9×N, N stands for the total number of RFs from the original database). We then estimate the stacking amplitude for each new dataset. The stacked amplitude from all bootstrapping sessions are expected to be distributed around the true value[1]. The average resulting amplitude in each bin is then obtained as the average of the trails, $\overline{\mathrm{Amp}} = \frac{1}{\mathrm{M}}\sum_{\mathrm{i}=1}^{\mathrm{M}} \mathrm{Amp_i}$, where $\mathrm{Amp_i}$ is the amplitude corresponding to the ith bootstrapping, and M is the number of bootstrapping trails (M=2000) for this study. The corresponding standard deviation is calculated using $\sigma = \sqrt{\frac{1}{\mathrm{M}-1}\sum_{\mathrm{i}=1}^{\mathrm{M}}(\mathrm{Amp_i} - \overline{\mathrm{Amp}})^2}$. In Fig. S4, the left panels show the CCP stacking waveforms with the 95% confidence level shaded, and the right panels only highlight the signals beyond the 95% confidence level. Our uncertainty analysis indicates that the phases X1 and X2 are robust features beyond the noise level.

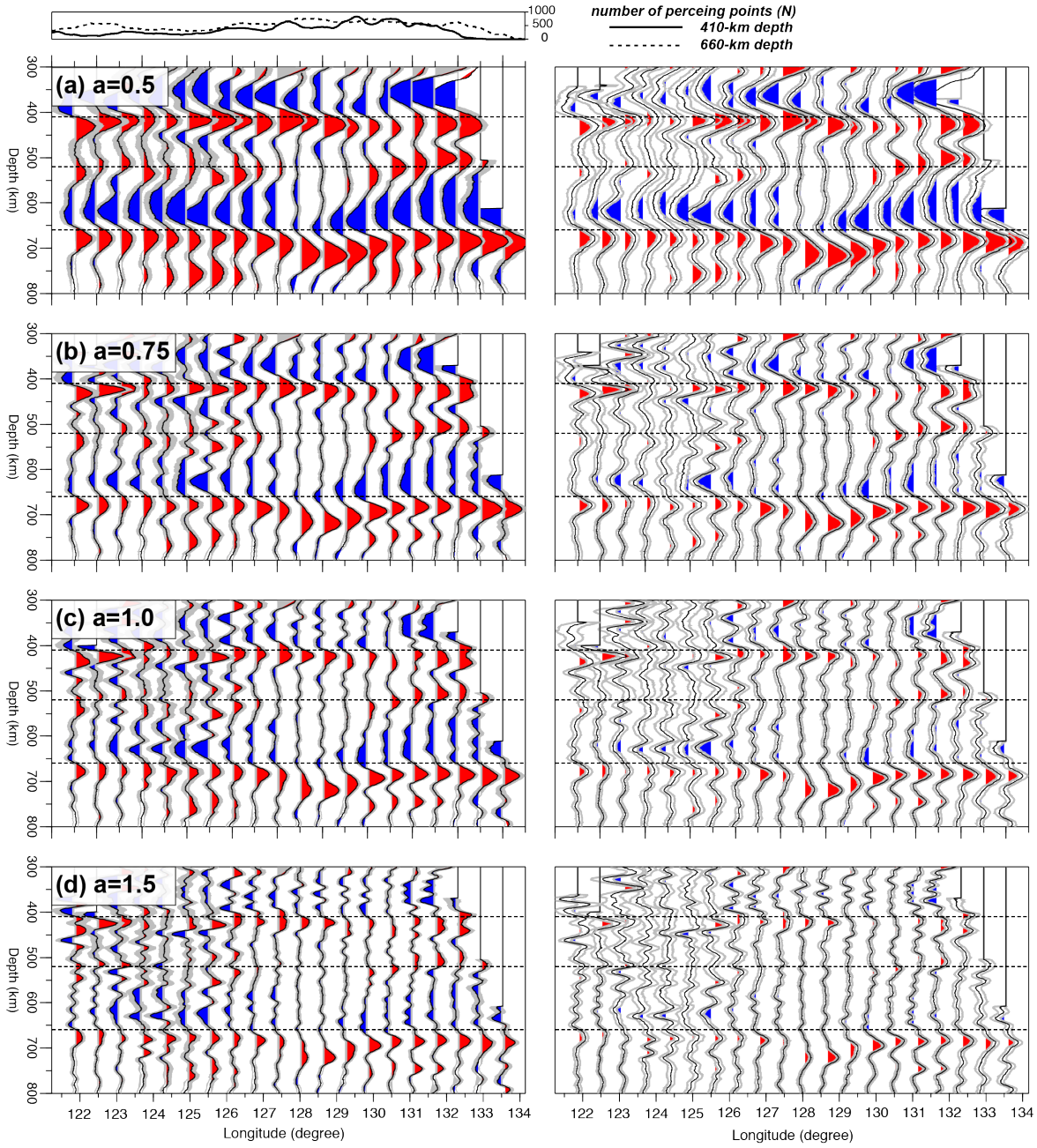


**Fig. S4.** Noise level estimated by a bootstrapping method. The left panels show the CCP stacking waveforms with the 95% confidence level shaded in gray. The right panels only highlight the signals beyond the 95% confidence level. Numbers of RF in each bin used in the CCP stacking at 410-km and 660-km depths are plotted at top. **(a)-(d)** shows the results in different frequency bands (different Gaussian low parameter).

## 4. Side-lobes on RFs caused by data processing

With the synthetic data, we also estimate the amplitudes of the side-lobes induced by the data processing in different frequency bounds using the synthetic data. We use the 1D IASP91 model[2] as our reference model and generate full waveform synthetic seismograms using the GPU-based 2D finite difference method[3], accurate up to 1 Hz. We then compute the RFs and construct the CCP stacking images for the synthetic seismograms in the same manner as the real data. Fig. S5 shows the CCP stacking images at difference frequency bands, with the stacked waveforms superimposed. The amplitudes of the side-lobes due to the data processing are in general small. In addition, in the real data (Fig. 2 in the main text), the positive amplitude phase X1 could not be a side-lode of the P410s phase, as it has the same polarity with the P410s. The negative phase X2 is not a side-lode of the P660s phase because (1) we do not observe a signal with similar amplitude under the P660s phase, (2) the phase X2 is dipping to the west with a dip angle around 25 degrees, while the P660s is almost flat. Thus the distance between phase X2 and P660s varies with the location. With all the above evidences, we conclude that phases X1 and X2 are not caused by the side-lobes in data processing.

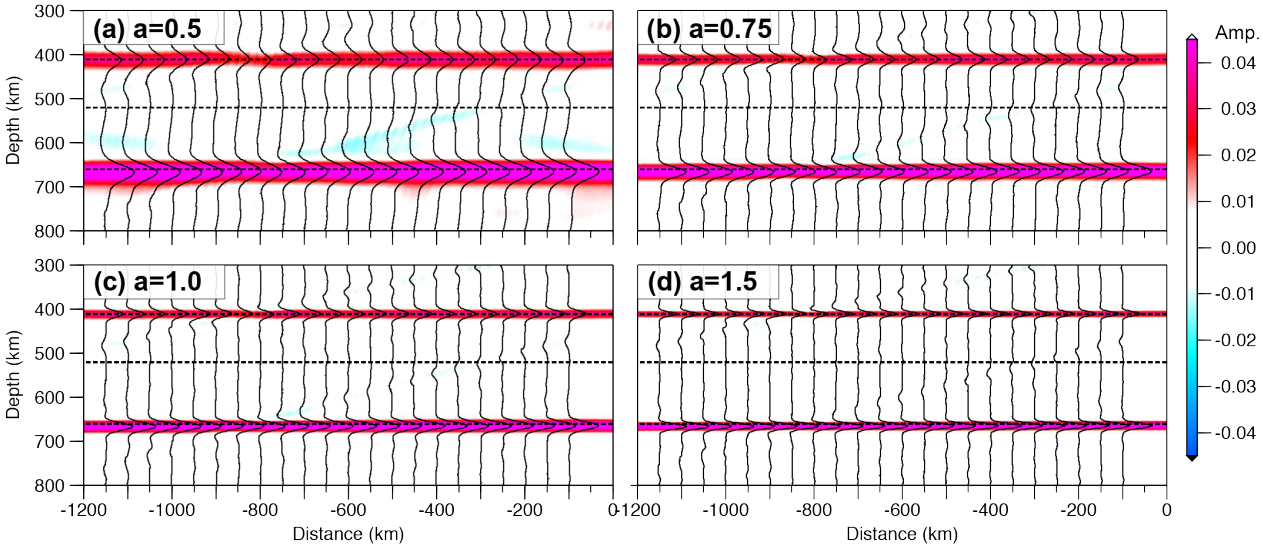


**Fig. S5.** Synthetic tests to understand the amplitude of the side-slopes due to the data processing. **(a)-(d)** shows the CCP stacking images conducted at different frequency bands. For better illustration, the stacked waveforms are superimposed.

## 5. Shallow structures' effect on MTZ RF study

The multiples generated by shallow structures may produce artifacts at MTZ depth. In this section, we conduct a series of 2D synthetic tests to understand the shallow structures' effect on MTZ RF study.

One of the dominant tectonic features in the northeast China is the Songliao basin, with reported sedimentary thickness[4] up to 7 km (Fig. S6a). We choose a W-E profile across the deepest part of Songliao basin (Fig. S6, profile C) to investigate the basin effect on MTZ RF study, even though the profiles shown in main text is far from basin (Fig. S6, profiles A and B). Our 2D model composed of the background velocity model from the IASP91[2], superimposed by a 50 km shallow velocity structures extracted from a tomographic model obtained through a joint inversion of the RF waveforms and surface-wave dispersions[5] (Fig. S6b). We obtain the 2D full-waveform synthetic seismograms using the 2D finite different method for six earthquakes, with three on each side of the array with epicentral distance of ~30/60/90 degrees. The station spacing is 10 km along the profile. We then compute the RFs and construct the CCP stacking image for the synthetic data in the same manner as the real data. The CCP stacking image shows that the existence of shallow basin will produce strong coda in the upper mantle, while the amplitude of coda decreases rapidly with the increasing of depth (Fig. S7). Given to the current understanding of the shallow crustal velocity structure[5], the basin does not produce strong multiples at the MTZ depth.

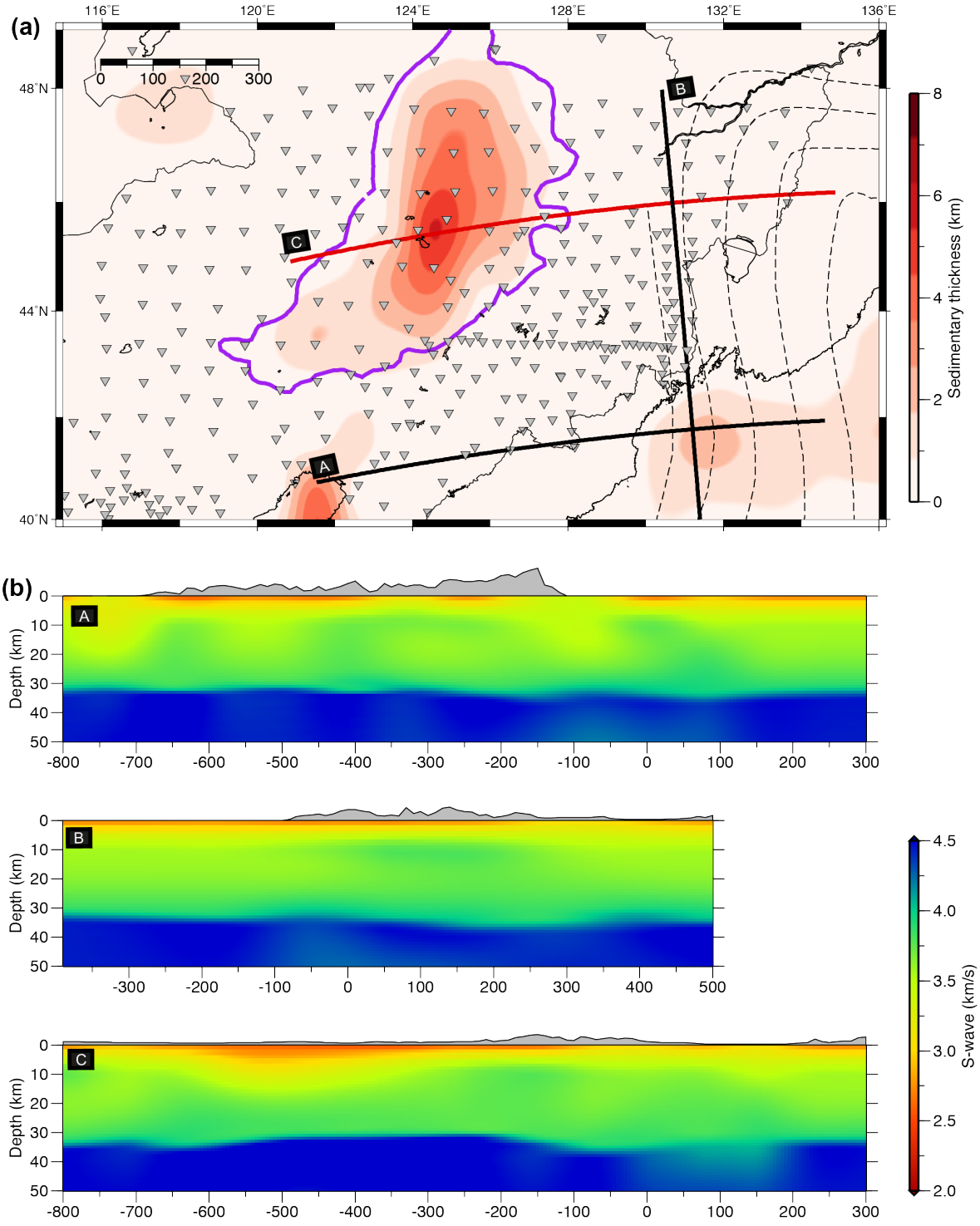


**Fig. S6. (a)** Map view shows the basin thickness from the CRUST 1.0 model[4]. The thick black lines A and B give the profile locations shown in main text. The profile C, an W-E profile across the deepest part of Songliao basin, is used to test the basin effect on MTZ RF study. **(b)** Depth profiles show the shear-wave velocity from Guo et al.[5].

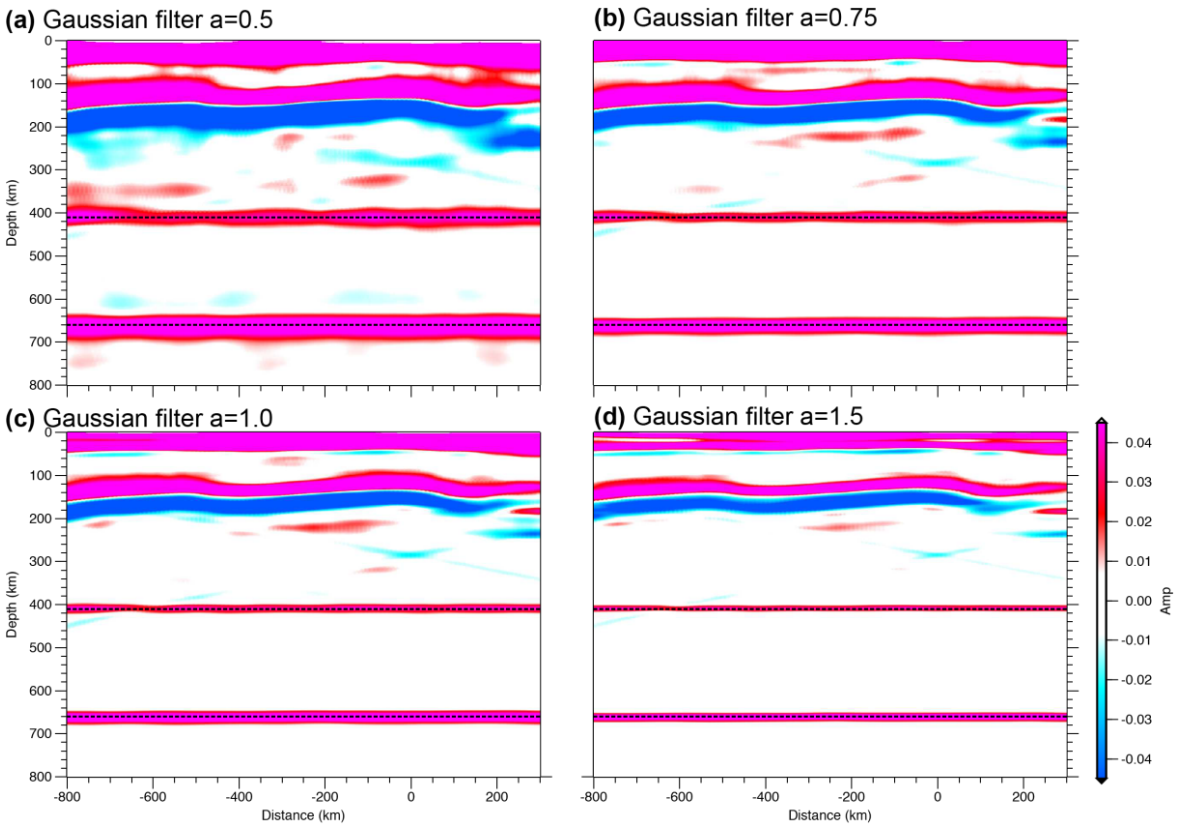


**Fig. S7.** The effect of crustal-scale structure on MTZ RF study at different frequency bands. The profile location is shown in Fig. S6 (Profile C). The corresponding input velocity model at shallow depth is given in Fig. S6b.

We acknowledge that the shear-wave speeds within the basin are likely over-estimated in the current tomographic models[5] (minimum Vs of 2.6 km/s) due to the limited station coverage and the usage of long-period waveforms. Thus, we conduct another type of synthetic test with the basin geometry from the CRUST 1.0 model[4] and the shear-wave velocity within the basin changing as a function of depth (linear change with Vs of 1.5 km/s at the surface to 2.5 km/s at the deepest part of the basin) (Fig. S8). There is a first-order velocity discontinuity between the basin (2.5 km/s) and basement rock (3.36 km/s). Due to the slow shear-wave velocity, the waveforms are trapped within the basin for a longer time with larger amplitude. 2D synthetic test indicates strong basin effect at the MTZ depth (Fig. S8). In this case, there are strong multiples within the MTZ depth, and most of these signals are located right beneath the basin. However, in the real data (Fig. 2), the phases X1 and X2, especially the dipping section (Fig. 3), do not correlate with the geographical location of the basin. In addition, these profiles are located far

from the basin (Fig.1). Thus, we conclude that the phases X1 and X2 are not caused by the sallow basin effect.

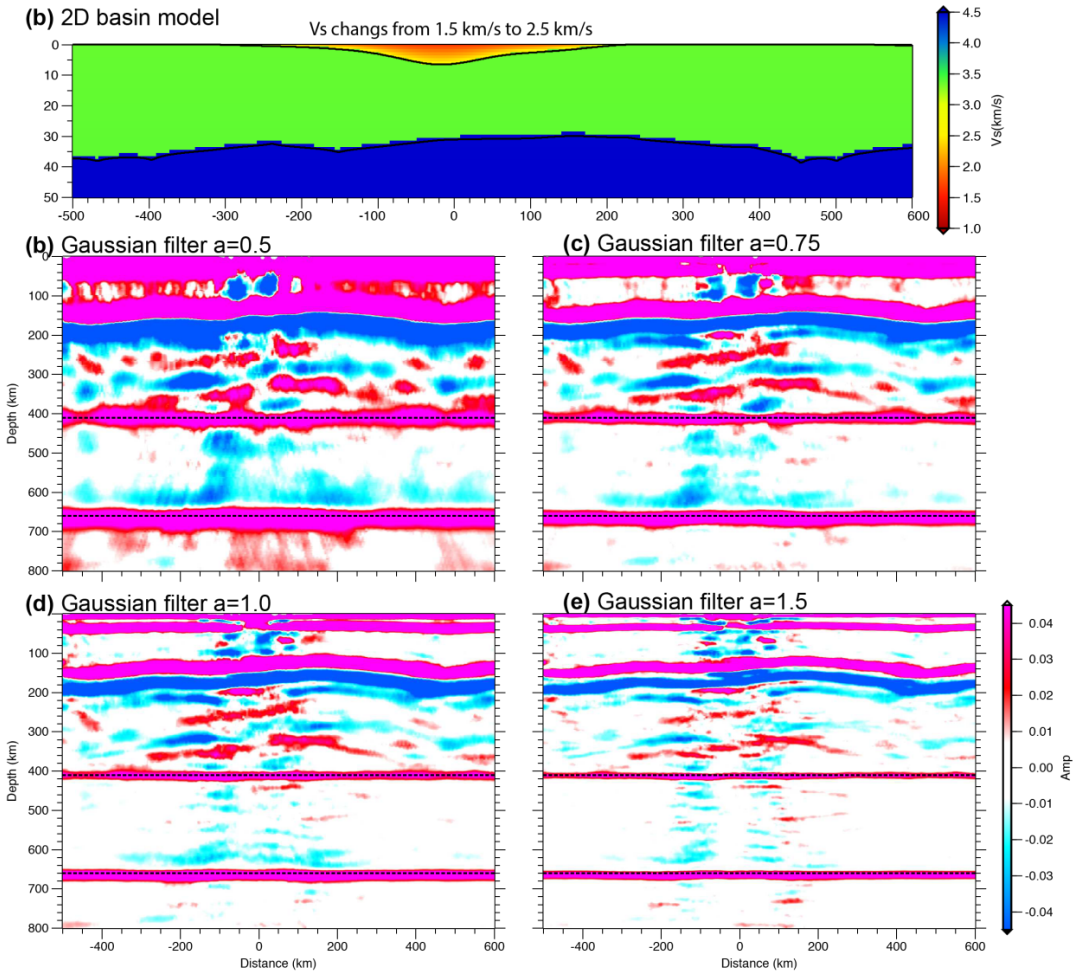


**Fig. S8.** The effect of crustal-scale structure on MTZ RF study. The input velocity model is shown in **(a)**. **(b)–(d)** show the RF stacking images constructed at different frequency bands.

In this section, we also test whether the phases X1 and X2 are multiples of the Lithosphere-Asthenosphere Boundary (LAB) located in the uppermost mantle. Based on recent S-wave RF study in northeast China, the average LAB is located at a depth of 120 km. We use a modified IASP91 model with a sharp LAB at ~120 km[6] (Fig. S9a) in our synthetic test. The synthetic tests show that negative multiples of the LAB emerged at ~380 km and positive multiples appeared at ~520 km depth, especially at low frequency range (Fig. S9b-d). This indicates that the interpretation of the low velocity zone about the 410 discontinuity should take into considering the effect of the LAB's multiples seriously. From our synthetic tests, there is also a very weak

(compare to the amplitude of the P410s and P660s) negative signal at ~600 km, though the signal only shows up at low frequency ranges. In contrast with the multiples from the LAB, the observed X2 phase in real data has large amplitude, which can be as strong as those from P410s (P660s) (Fig. 2). In addition, phase X2 appears at both long period and high frequencies (Fig. 2). Thus, we argue that phase X2 is not caused by the multiples from the LAB.

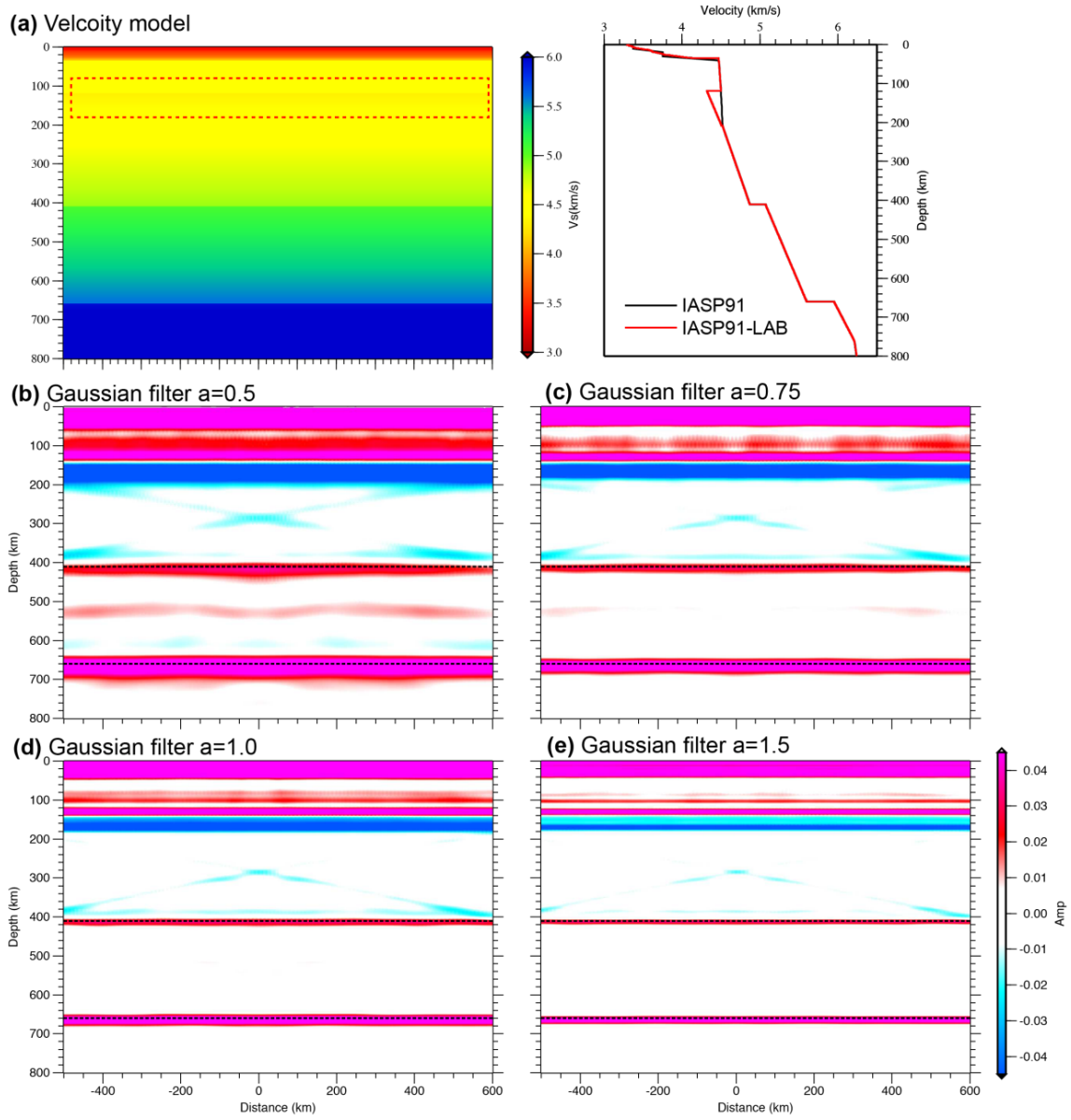


**Fig. S9.** The effect of Lithosphere-Asthenosphere Boundary (LAB) structure on MTZ RF study. The input velocity model is given in **(a)**. **(b)–(d)** show the RF stacking images constructed at different frequency bands.

## 6. 2D synthetic tests using tomography or geothermal model

In this section, we first test whether the strongly smoothed velocity anomalies in current tomography models can produce observed phases X1 and X2. Our 2D model set up includes the background velocity model from the IASP91[2], superimposed the velocity perturbation of regional high-resolution tomography model from Tang et al.[7] (Fig. S10a and S10b). We generated 2D synthetic seismograms and obtained CCP stacking image in the same manner as the real data, including corresponding travel time corrections using the tomographic results. Figures S10c and S10d show the CCP stacking image before and after applying the velocity correction, respectively. Before velocity correction, the topography of thed410 and d660 display a certain degree of fluctuation, which is expected as the depth of d410 and d600 are strongly affected by the upper mantle velocity heterogeneities. After velocity correction, the depth of the d410 and d660 are well recovered, demonstrating the accuracy of our velocity correction approach. In addition, we found that the strongly smoothed velocity anomalies in current tomography models are unable to generate the phases X1 and X2 to match our observations.

We also test whether the phases X1 and X2 can be caused by the thermal gradient of the subducting slab, as there is a distinct temperature difference between the slab and surrounding mantle. We consider a typical subduction geothermal model in northeast China[8,9], where the coldest core of the slab is about 1000 K lower than the surrounding mantle, which is much larger than current seismological observations (Fig. S11). We estimate the 2-D velocity anomalies due to the thermal effect using a temperature-velocity relationship[10] of $\mathrm{dVs/dT} = -3.1 \times 10^{-4}\ \mathrm{km\ s^{-1}K^{-1}}$, resulting in a maximum velocity anomaly of ~8%. By considering the dipping structure effect on RF study[11], we use three earthquakes with incidence from the slab downdip direction to explore the maximum possible RF energy. We then construct the synthetic CCP stacking images using the same manner as the real data. Our 2D synthetic test shows that the temperature anomaly in current model can produce strong seismic energy within the MTZ at the low frequencies, but can't generate strong signals in the high frequencies (Fig. S12c-f). This is mainly due to the thermal gradient of the slab (~150 km) is not sharp enough[12]. In comparison, our multiple-frequency RF waveform modelling suggests that the phase X2 is corresponding to an interface with gradient over 20-50 km.

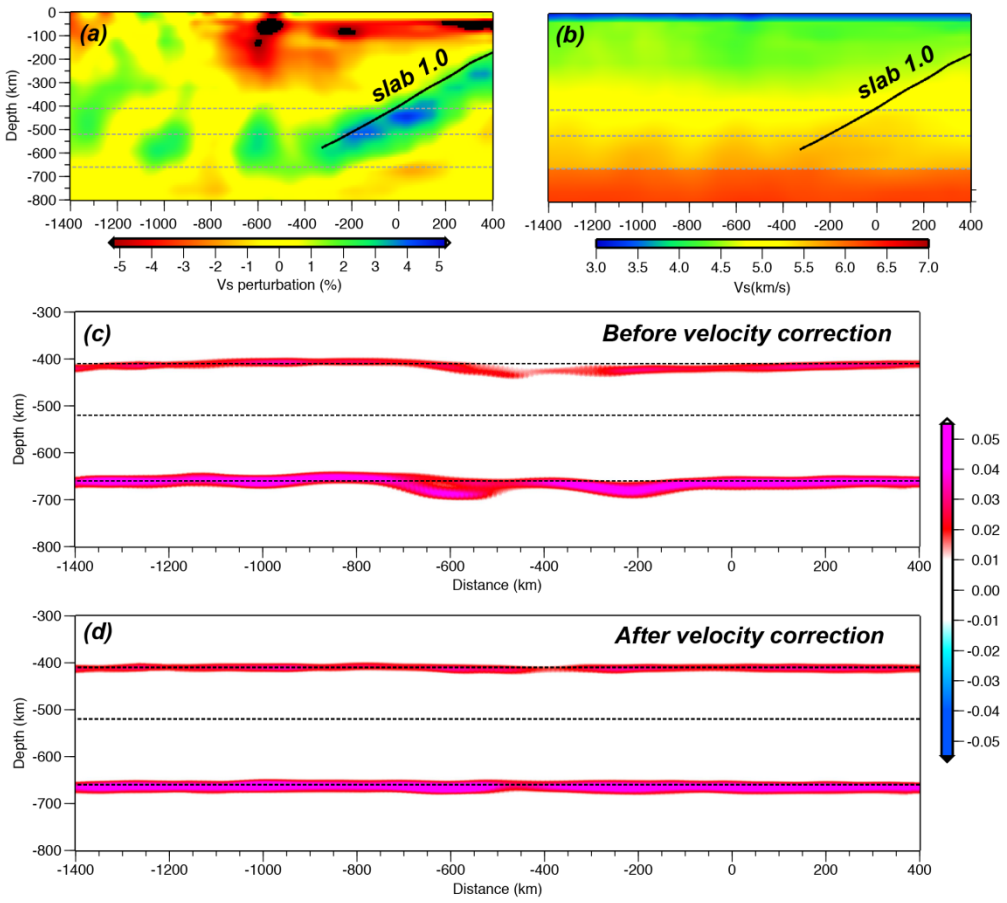


**Fig. S10. (a)** Shear-wave velocity perturbation from Tang et al.[7]. **(b)** Absolutely velocity model used in the 2D synthetic test. **(c)** and **(d)** shows the 2D synthetic CCP stacking images (Gaussian parameter a = 1.0) before and after 2D velocity correction, respectively.

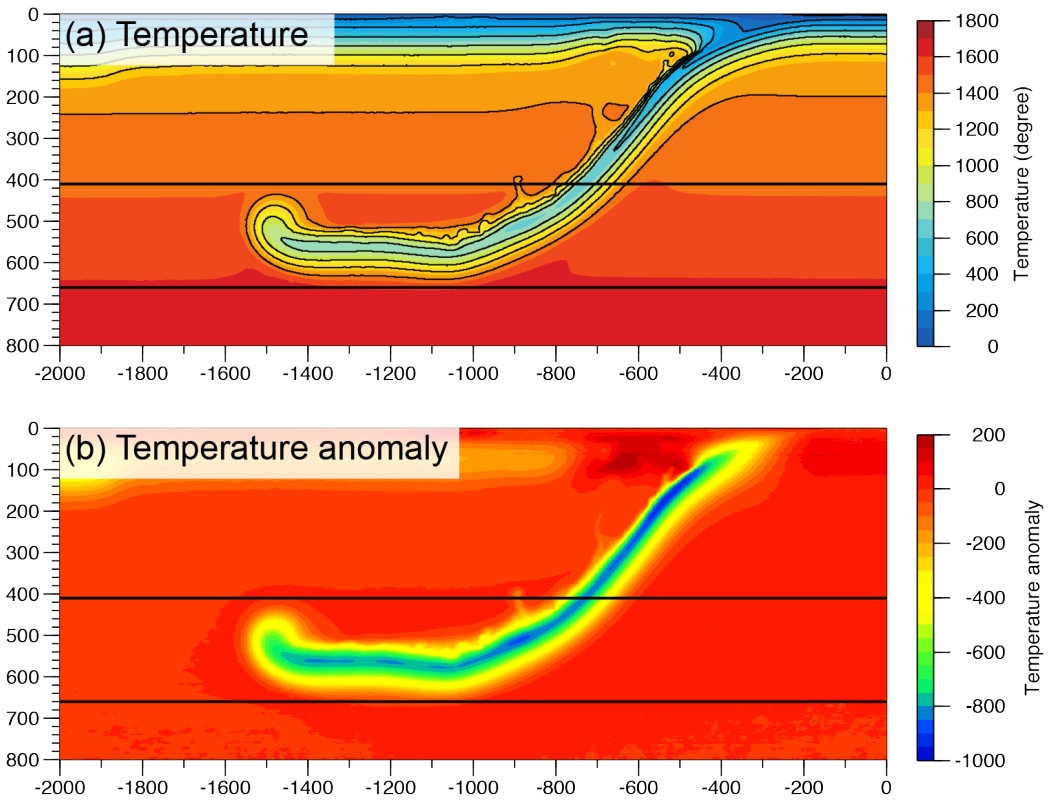


**Fig. S11.** Thermal (a) and thermal anomalies (b) of the slab model used in our 2D synthetic test[9].

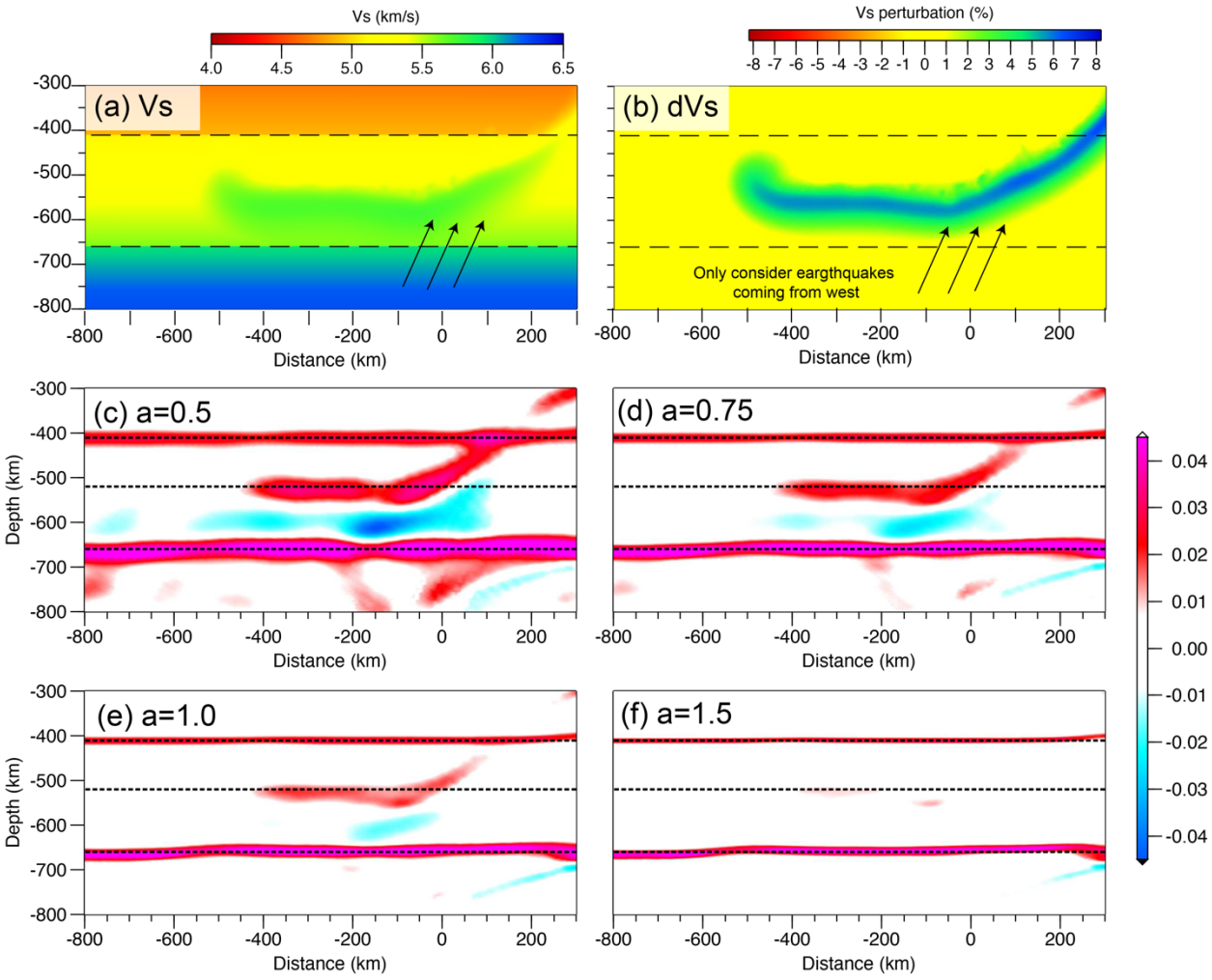


**Fig. S12. (a)-(b)** Shear-wave velocity and velocity anomalies of the slab model used in our 2D synthetic test. **(c)–(f)** show the CCP stacking images conducted at different frequency bands.

## Reference:


1. Efron, B. & Tibshirani, R. Statistical Data Analysis in the Computer Age. *Science* **253**, 390–395 (1991).
2. Kennett, B. L. N. & Engdahl, E. R. Traveltimes for global earthquake location and phase identification. *Geophys. J. Int.* **105**, 429–465 (1991).
3. Li, D., Helmberger, D., Clayton, R. W. & Sun, D. Global synthetic seismograms using a 2-D finite-difference method. *Geophys. J. Int.* **197**, 1166–1183 (2014).
4. Laske, G., Masters, G., Ma, Z. & Pasyanos, M. Update on CRUST1. 0—A 1-degree global model of Earth's crust. (2013).

5. Guo, Z. *et al.* High resolution 3-D crustal structure beneath NE China from joint inversion of ambient noise and receiver functions using NECESSArray data. *Earth Planet. Sci. Lett.* **416**, 1–11 (2015).
6. Zhang, R., Wu, Q., Sun, L., He, J. & Gao, Z. Crustal and lithospheric structure of Northeast China from S-wave receiver functions. *Earth Planet. Sci. Lett.* **401**, 196–205 (2014).
7. Tang, Y. *et al.* Changbaishan volcanism in northeast China linked to subduction-induced mantle upwelling. *Nat. Geosci.* **7**, 470–475 (2014).
8. Zhang, Y. *et al.* Phase transitions of harzburgite and buckled slab under eastern China. *Geochemistry, Geophysics, Geosystems* **14**, 1182–1199 (2013).
9. Yang, J. *et al.* Slab-triggered wet upwellings produce large volumes of melt: Insights into the destruction of the North China Craton. *Tectonophysics* (2018).
10. Irifune, T. *et al.* Sound velocities of majorite garnet and the composition of the mantle transition region. *Nature* **451**, 814–817 (2008).
11. Schulte-Pelkum, V. & Mahan, K. H. A method for mapping crustal deformation and anisotropy with receiver functions and first results from USArray. *Earth Planet. Sci. Lett.* **402**, 221–233 (2014).
12. Tauzin, B., Kim, S. & Kennett, B. L. N. Pervasive seismic low-velocity zones within stagnant plates in the mantle transition zone: Thermal or compositional origin? *Earth Planet. Sci. Lett.* **477**, 1–13 (2017).